Received: 1 June 2020 | Revised: 6 July 2020 | Accepted: 11 July 2020

DOI: 10.1002/er.5820

Check for updates

RESEARCH ARTICLE

INTERNATIONAL JOURNAL OF ENERGY RESEARCH WILEY

Investigation of Ti-substitution effects on structural and electrochemical properties of $Na_{0.67}Mn_{0.5}Fe_{0.5}O_2$ battery cells

Serdar Altin[1] | **Sebahat Altundag**[1] | **Emine Altin**[2] | **Erdinc Oz**[3] | **Messaoud Harfouche**[4] | **Ali Bayri**[1]

[1]Physics Department, Inonu University, Malatya, Turkey

[2]Inonu University, IBTAM, Malatya, Turkey

[3]Chemistry Department, Bilkent University, Ankara, Turkey

[4]Synchrotron-light for Experimental Science and Applications in the Middle East (SESAME), Allan, Jordan

Correspondence
Serdar Altin, Inonu University, Physics Department, Malatya, Turkey.
Email: serdar.altin@inonu.edu.tr

Funding information
Inönü Üniversitesi, Grant/Award Number: FBA-2019-1857; TUBITAK, Grant/Award Number: 119M169; Inonu University

Summary

Ti-substituted $Na_{0.67}Mn_{0.5}Fe_{0.5}O_2$ powders were fabricated by quenching at high temperatures, and the structural properties were investigated by Fourier transform infrared (FTIR), Scanning Electron Microscope (SEM), X-ray powder diffraction (XRD), and X-ray absorption spectroscopy (XAS) measurements. According to XRD analysis, it was not observed any impurity phases and it was found that the lattice constants of the powders were slightly increased by Ti content. The change in the valence state of both Mn and Fe ions was investigated by X-ray absorption near edge structure (XANES), and it was found that Ti-substitution caused a decrease in the valance state of Fe in $Na_{0.67}Mn_{0.5}Fe_{0.5}O_2$. Fourier transform (FT) of XANES showed that the local structure around the metal ions changed with the addition of Ti ions. The cycling voltammetry (CV) graphs of Ti-substituted cells were almost the same as the pure sample, which may not change the cycling mechanism in the cells. According to galvanostatic cycling measurements at room temperature, the best performance was obtained with Ti-substitution of 0.06 to 0.09 in the structure. The effect of environmental temperature in the battery cells was investigated at 10°C to 50°C, and it was found that the battery performance depends on the environmental temperatures.

KEYWORDS

Na ion, $Na_{0.67}Mn_{0.5}Fe_{0.5}O_2$, Ti-substitution

1 | INTRODUCTION

In recent decades, battery technologies have developed very fast and commercial batteries have been used in electric vehicles to miniaturize electrically powered devices.[1,2] Li-based battery technologies are widely used in all electrically powered systems, and this could cause an increase in the demand for Li sources. In addition, it is well known that the reserves of Li are limited and the production cost increases with time.

Na-based electrode materials have huge potential for replacing Li ion batteries, and scientists have tried to develop Na-battery technologies for better electrochemical properties.[3,4] It is well known that Na is cheaper, environmentally friendly, and abundant on the planet. It is also well known that Li and Na ions have similar properties, and the chemical structures of Li-based electrode materials have been adapted to Na ions demonstrating similar electrochemical activity as Li-based structures.[5-8]

 © 2020 John Wiley & Sons Ltd

Among the Na-based metal-oxide electrode materials, Na–Fe–Mn–O electrode materials have special importance since Fe and Mn ions are cheap and abundant when compared to others. The Na–Fe–Mn–O battery was first discovered by Yabuuchi et al. in 2012, and it was found that there are P2-type and O3-type structures, which are easily fabricated by conventional production techniques, and the capacity values were found to be 190 mAh/g.[9,10] The reversible redox reaction of Mn and Fe ions in the structure was observed for 1.5 to 4.3 V, which causes the high capacity value in the cells.[11] It is well known that the crystal structure of the P2-type with P63/mmc symmetry and *the crystal structure of the O3-type with R-3 m structure* have two and three different Na sites in their lattices, respectively.[12]

There are some problems in $Na_{0.67}Mn_{0.5}Fe_{0.5}O_2$ cells, and it has been observed that capacity fade is the main problem in the battery cells.[13] Furthermore, Singh et al. found that Na-ion mobility in the cells decreases with increased cycling.[14] It has been stated that the environmental conditions directly affect the structural properties of $Na_{0.67}Mn_{0.5}Fe_{0.5}O_2$.[15]

It is stated that structural stabilization of $Na_{0.67}Mn_{0.5}Fe_{0.5}O_2$ phase can be provided by the partial substitution of transition metal oxide in the structure. In the literature, researchers tried to improve $Na_{0.67}Mn_{0.5}Fe_{0.5}O_2$ cathode by doping/substituting with Ni, Ti, Co, Al, Cr, Mg, etc.,[11,15-20] and it is seen that the crucial number of impurity ions in the lattice causes the improvement of the Na-diffusion rate during the charge and discharge. In this case, the electrostatic force of the substituted ions which have a different charge value from original ions will change and it may increase the stability of the lattice during the cycling. It is stated that small amount of Ti-substitution in lithium nickel cobalt aluminium oxides (NCA), lithium nickel cobalt manganese oxides (NCM), and $LiFeSO_4F$ cathodes gives better battery performance.[21-23] Similarly, Park et al found that small amount of Ti for both Mn and Fe sites in $Na_{0.67}Fe_{0.5}Mn_{0.5}O_2$ gives better electrochemical results.[19] So it is well known that Ti-ions in the sodium transition metal oxide structure give an improvement in the battery cells. So the systematic investigation of the Ti-substitution in $Na_{0.67}Fe_{0.5}Mn_{0.5}O_2$ is important for Na-ion battery studies. In addition to this, the battery performance for diffferent temperatures is also important for determination of the capacity change with enviromental temperature. In this study, we successfully fabricated Ti-substituted $Na_{0.67}Mn_{0.5}Fe_{0.5}O_2$ powders. The structural properties were investigated by FTIR, SEM, XRD, and XAS, and the battery performance was investigated in detail. The systematic Ti-substitution effects in electrochemical properties and battery performance for different environmental temperatures were investigated.

2 | EXPERIMENTAL SECTION

To fabricate Ti-substituted $Na_{0.67}Mn_{0.5}Fe_{0.5}O_2$ powders, Na_2O_2, Fe_2O_3, TiO_2, and Mn_2O_3 were used as starting powders. They were weighed on a Radwag sensitive balance, and an agate mortar was used for mixing the powders for 1 to 1.5 hours in an argon-filled glove box. They were then pressed under 5 tons to obtain the pellet form of the powders. The pellets were placed in an α-Al_2O_3 crucible and heated at 1000°C for 6 hours under room conditions, and they were quenched in liquid N_2.

Thermogravimetric (TG) and Differential Thermal Analysis (DTA) analysis of the powders from room temperature to 950°C were performed with a SHIMADZU DTG-60AH under an oxygen gas atmosphere.

The XRD measurements were performed with Rigaku RadB Dmax diffractometer with CuK_α ($\lambda_{K\alpha}$ = 1.5405 Å) radiation. The lattice parameters were calculated with the GSAS-II open-source program.[24,25] FTIR analyses were performed with a Perkin Elmer, Spectrum One model, in the range of 400 to 4000 cm^{-1}. The XAFS experiments of the samples were performed in the XRF/XAFS Beamline at SESAME-Jordan. The surface morphology was investigated with a Leo EVO-40 VPX SEM and BRUKER X-flash detector 4010 energy-dispersive X-ray spectroscope (EDX).

CR2032 coin cell cases were used for the electrochemical investigations. The super carbon, polyvinylidene fluoride (PVDF), and active materials (15:15:70) were mixed in N-Methyl-2-pyrrolidone (NMP) in a glass tube with a magnetic stirrer for 24 hours at room temperature, and then the mixtures in the gel form were coated onto aluminum foils with a doctor blade with a 100 μm coating size and placed in a vacuum furnace at 110°C for 24 hours. The coated Al film was pressed with a rolling press and punched with a diameter of 10 mm and stored in an argon-filled glove box (Inert Technology, I-Lab). The mass of active materials in the CR2032 coin cells was in the range of 2.0 mg to 3.0 mg. The pure Na metal was used as an anode, and an electrolyte of 1 M $NaClO_4$ in propylene carbonate (PC) / ethylene carbonate (EC) (50/50 w) was preferred in the cells.

The CV measurements of the cells were performed between 1.5 V and 4.0 V at a scan rate of 0.1 mV/s, and the galvanostatic cycling process was measured at the same voltage window with CV for the C/3-rate by Ivium Octostat30 at room temperature. Brunauer–Emmett–Teller (BET) surface area was measured by a TriStar 3000 (three port) surface analyzer (Micromeritics USA).

The temperature dependence of the galvanostatic charge/discharge up to 100 cycles of the cells was measured with aZive SP1 integrated NUVE EN-120 incubator.

3 | RESULTS AND DISCUSSION

The DTA and TG of Ti-substituted samples from room temperature to 950°C using a heating rate of 10°C/min are given in Figure 1A, B, and it should be noted that the endothermic peaks (signed as P_1-P_5) below 450°C may be due to decompositions of the Na_2O_2, Fe_2O_3, TiO_2, and Mn_2O_3 starting materials. The signed peaks at P_6 may be related to the first formation of the non-stoichiometric Na–Mn–Fe–O phase, and the P_7 region should be due to the $Na_{0.67}Mn_{0.5}Fe_{0.5}O_2$ phase. Therefore, it is seen that the $Na_{0.67}Mn_{0.5}Fe_{0.5}O_2$ phase can be fabricated above 900°C by the solid-state reaction technique using the starting materials given in the experimental section.[12] **Figure 1B** presents the TG curve of the Ti-substituted samples, and a mass loss in the samples as the temperature increased was observed. The mass loss of ~7% between 65°C and 105°C, which is designated as R_1 in the graph, was related to the degradation of Na_2O_2 and the release of oxygen and evaporation of water in Fe_2O_3.[25-27] The mass loss in the R_2 region should be due to Mn_2O_3.[28] The R_3 region in the TG curve may be related to the release of excess oxygen and Na evaporation in the formation of $Na_{0.67}Fe_{0.5}Mn_{0.5}O_2$ in the structure since there should be oxygen gas released according to the chemical reaction given below:

$$\frac{1}{3}Na_2O_2 + \frac{1}{4}Mn_2O_3 + \frac{1}{4}Fe_2O_3 \rightarrow Na_{0.67}Fe_{0.5}Mn_{0.5}O_2 + \frac{1}{12}O_2$$

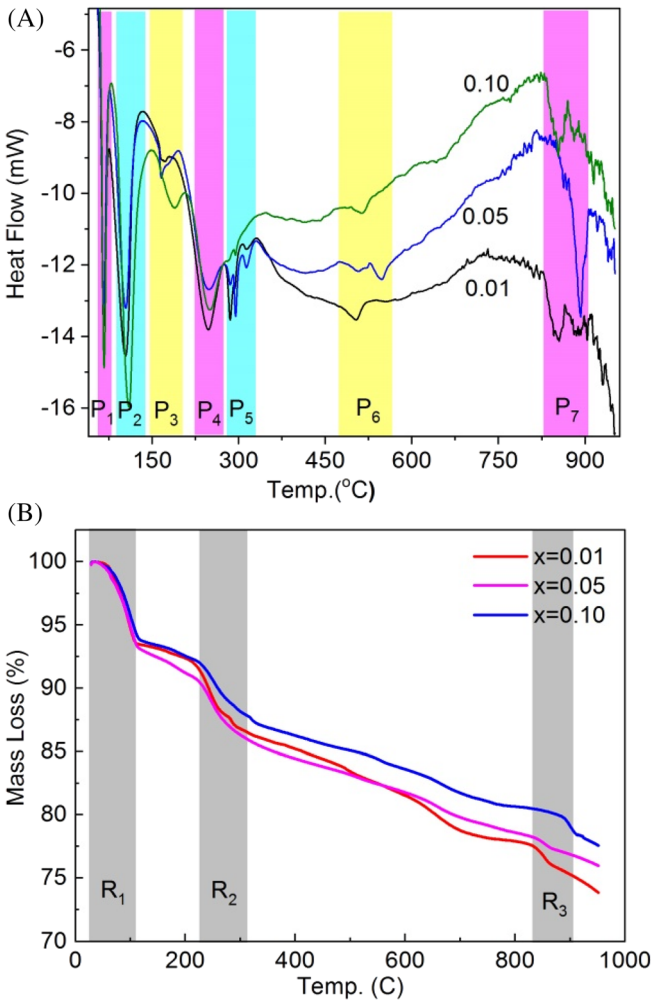


FIGURE 1 (A) DTA and (B) TG of Ti-substituted $Na_{2/3}Mn_{0.5}Fe_{0.5}O_2$ [Colour figure can be viewed at wileyonlinelibrary.com]

Figure 2A presents the XRD of the Ti-substituted $Na_{0.67}Fe_{0.5}Mn_{0.5}O_2$ samples, and it is seen that the XRD patterns of the powders matched with the PDF card numbered 00-0027-0751.[20] No impurity phases were observed in the Ti-substituted samples. Therefore, it can be stated that Ti for all samples was dissolved in the structures which indicates successful substitution of Ti with Fe ions.

The lattice parameters of the Ti-substituted samples were calculated using the open-source GSAS-II program, and Figure 2B shows the XRD of the experimentally obtained curves, theoretically calculated curves, and difference curves for x = 0.04. The unit cell parameters of the powders are presented in Figure 2C, and it can be seen that both lattice parameters increased with increasing Ti content in the structures. To understand the change in the lattice parameters, we compared the ionic radii of Ti and the other ions in the structure. The chemical formula may be written as $Na^{1+}{}_{0.67}(Fe^{3}{}_{2/3}Fe^{4}{}_{1/3})_{0.5}(Mn^{3}{}_{2/3}Mn^{4}{}_{1/3})_{0.5}O^{2-}{}_{2}$, and the ions of Mn^{3+} (64.5 pm), Mn^{4+} (53 pm), Fe^{3+} (64.5 pm), and Fe^{4+} (58.5 pm) are expected in the structure.[29] The ionic radii of Ti^{2+}, Ti^{3+}, and Ti^{4+} are 86, 67, and 60.5 pm, respectively.[30] It was found that Ti^{4+} substitution with Fe^{4+} ions caused an increase in the lattice parameters of the cells.

Figure 3 presents the FTIR spectra of Ti-substituted $Na_{0.67}Fe_{0.5}Mn_{0.5}O_2$ powders. The P_1 region is due to the Fe–O bonds and bending of the Na–O bonds.[31,32]The P_2 region is related to Fe–O–Fe,[33,34] and P_3 and P_5 peaks were assigned to Mn–O and Fe–O, respectively.[35] FTIR peaks of TiO_2 were observed at 540 cm^{-1} (P_1 region), 660 cm^{-1} (P_1 region), 1608 cm^{-1} (P_4), and 3451 cm^{-1} (P_5 region).[36] Therefore, extra peaks due to overlapping of the TiO_2 peaks by $Na_{0.67}Fe_{0.5}Mn_{0.5}O_2$ were not observed in the FTIR spectra.

SEM images of x = 0.01, 0.05 and 0.1 were given in Figure 1A-C, and it is seen that the grain structure shows similar formation. The EDX dot mapping of x = 0.07 as an example was given in Figure 4D. The elemental distribution of x = 0.07 was obtained as Na/Mn/Fe/Ti = 40.85/30.62/24.49/4.04. The theoretical expectation of $Na_{0.67}Mn_{0.5}Fe_{0.5}O_2$ is Na:Mn:Fe:Ti = 40.12/29.94/25.75/4.19,

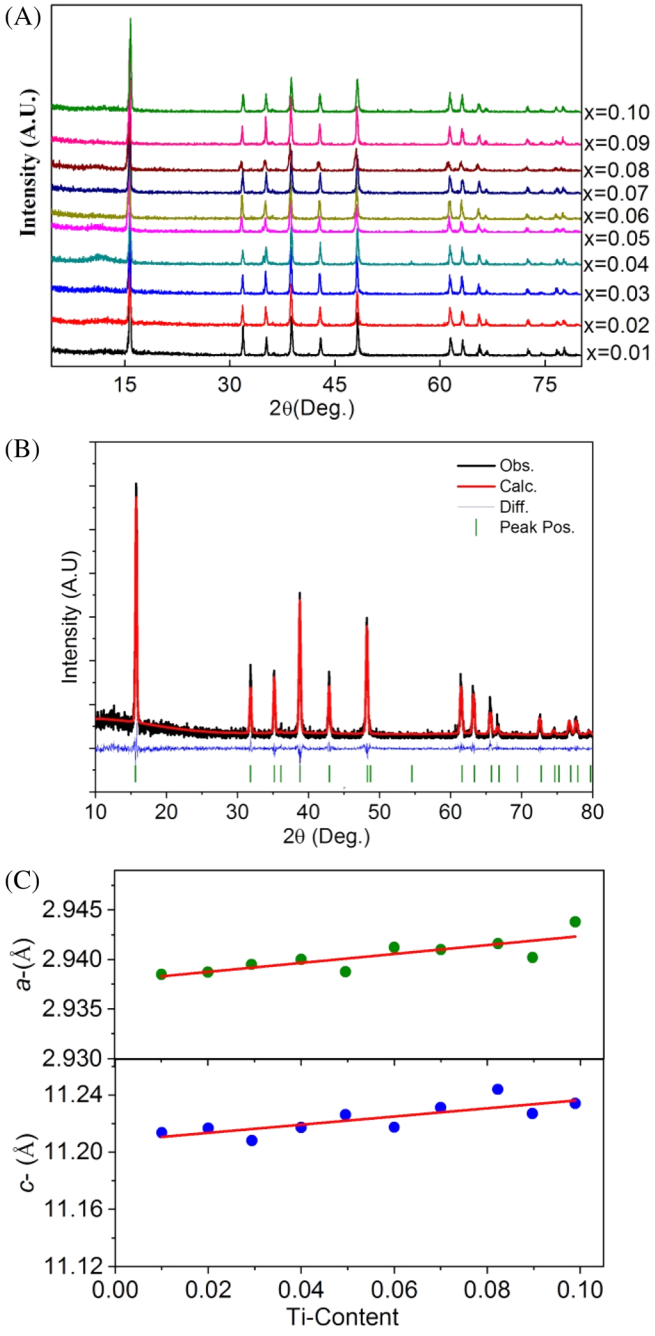


FIGURE 2 (A) XRD patterns of Ti-substituted powders, (B) results of Rietveld refinement for x = 0.04, and (C) lattice parameters depending on the Ti-content. The R_w parameters after fitting were obtained as 24.8, 22.1, 22.9, 23.8, 25.7, 23, 24, 26.6, 24.2, and 23.9 for x = 0.01-0.1 [Colour figure can be viewed at wileyonlinelibrary.com]

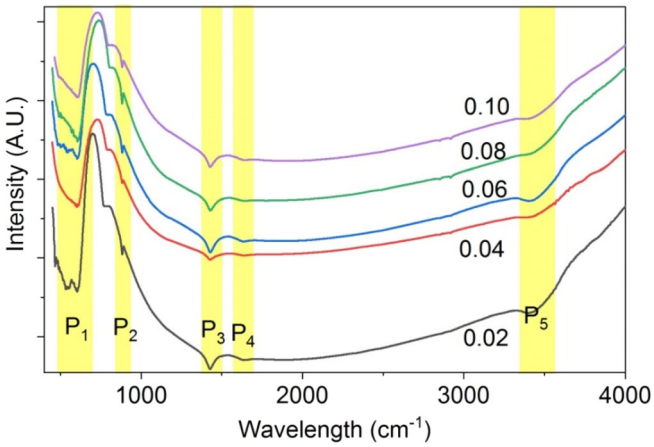


FIGURE 3 FTIR of Ti-substituted $Na_{0.67}Fe_{0.5}Mn_{0.5}O_2$ [Colour figure can be viewed at wileyonlinelibrary.com]

so the experimental results are in good agreement with theoretical calculation. The ImageJ open source program was used for calculations of grain size, and a 15 μm × 15 μm area was used for the calculation.[37-39] **Figure 4E** shows the grain size distributions of the Ti-substituted sample with x = 0.01 calculated from the SEM images. Since all powders have similar surface morphology, we did not present the SEM images and particle size distribution graphs of all samples in the figure. The average particle size distributions are given in Figure 4F, and it can be seen that Ti-substitution caused an increase in the grain size of the samples, and this may be due to the thermodynamic nature of the grain formations. To understand the grain formation by Ti-substitutions, phenomenological kinetic grain growth model should be considered as below:

$$G^n = K_0 t \cdot \exp(-Q/RT)$$

Where G is the average grain size at time t, n is the kinetic growth exponent, K_0 is the pre-exponential term, Q is the activation energy, R is the ideal gas constant, and T is the absolute temperature.[40] The substitution studies show that the Q and n terms directly change with structural modification.[41] So, we predicted that the Ti-substitution in $Na_{2/3}Mn_{0.5}Fe_{0.5}O_2$ causes the decrease of the n or/and Q values.

The XANES Mn K-edge spectra of Ti-substituted $Na_{2/3}Mn_{0.5}Fe_{0.5}O_2$ powders are given in Figure 5A. When the existing XANES spectra of Mn^{2+}, Mn^{3+}, and Mn^{4+} were considered,[42-44] it was found that the Ti-substituted $Na_{0.67}Mn_{0.5}Fe_{0.5}O_2$ had Mn^{3+} and Mn^{4+} valence states in the structure. In addition, it should be noted that the shoulder in the spectrum around 6553 eV was decreased to lower energy by Ti-substitution which may be caused by the increase of the number of Mn^{3+} in the structure. Although we indirectly concluded the increase of the number of Mn^{3+}, the determination of the real number of Mn^{3+}should be performed by XPS. Figure 5B shows the Extended X-Ray Absorption Fine Structure (EXAFS)

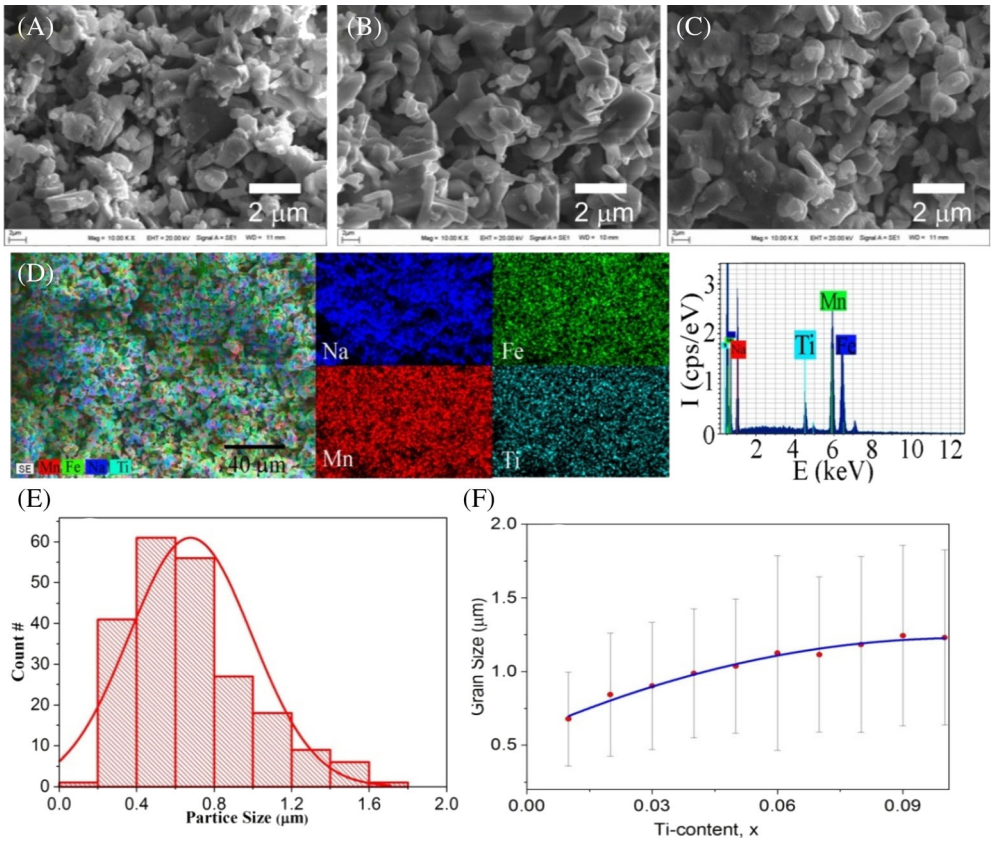


FIGURE 4 SEM images of (A) x = 0.01, (B) 0.05, and (C) 0.1, (D) EDX dot mapping results of x = 0.07 sample, (E) the grain size of calculation from SEM by ImageJ for x = 0.07, and (F) depending on the Ti-content [Colour figure can be viewed at wileyonlinelibrary.com]

data, and the Fourier transform of the signal of Ti-substituted powders has two main peaks around 1.9 Å and 2.9 Å, and the second peak increases with increasing Ti-substitution. To determine the exact bond lengths, we fitted the FT of the EXAFS data, as seen in Figure 5d, and the obtained values are given in Table 1. Although it is seen that the Mn–O bond length did not change with Ti-substitution, the Mn–Metal (Fe or Ti) bond length increased, as seen in Figure 5c and Table 1. We concluded that the decrease in the number of Mn^{4+} ions caused the decrease in the electrostatic force between the metal ions, which may have increased the bond length.

Figure 5E presents the XANES Fe-edge spectra of x = 0.03, 0.05, 0.07, and 0.01 powders. It is well known that the Fe K-edge with different valence states changes the energy regions, and the peak of the XANES of Fe^{4+} is located between Fe^{2+} and Fe^{3+} spectra.[45,46]The XANES Fe-edge spectra of the samples is mainly composed of Fe^{3+} spectra. We believe that the change around 7125 eV with Ti-substitutions is due to the existence of the Fe^{4+} ions in the structure. Although Park et al found that there are Fe^{2+} and Fe^{3+} ions in the structure which were observed in the XPS study,[19] Bai et al and Marelli et al stated that there are Fe^{3+} and Fe^{4+} ions in $Na_{2/3}Mn_{0.5}Fe_{0.5}O_2$.[47] Therefore, we come to conclusion that there are Fe^{3+} and Fe^{4+} ions in the structure. The Ti^{4+} substitution by Fe ions in the structure should increase the number of Fe^{3+} ions due to the charge equilibrium of $Na_{0.67}Mn_{0.5}Fe_{0.5}O_2$. Therefore, the main structure of the XANES Fe K-edge spectra did not change with Ti-substitution, and the change around 7125 eV may be due to the decrease in the number of Fe^{4+} ions in the structure.

According to Rietveld refinement of the XRD data, the first peaks are due to the Metal (Fe/Mn/Ti)–O bond, the second peak is due to Metal–Metal and Metal–Na bonds, and the third peak is due to the Metal–Na and Metal–Metal bonds. Figure 5F presents the EXAFS data of Ti-substituted samples, and the Fourier transform of Figure 5G has two main peaks in the graphs. To determine the exact bond lengths, we fitted the FT of the EXAFS data, as seen in Figure 5H and the obtained values are given in Table 2. It can be observed that there are two different types of Fe–O bond lengths in the samples and one of the bonds of Fe–O was disappeared for x ≥ 0.05. When Fe^{3+}–O–Fe^{3+} bonds were in the structure and when $Ti^{4+}$was substituted with Fe^{3+}, Ti ions attracted the oxygen ions instead of Fe^{3+} due to the electrostatic force. Two different bond lengths should be observed in the structure, as shown in Table 2. When the number of Ti ions reached a crucial number, one Fe–O bond was observed in the structure. The Fe–M bond length increased slightly, which could be due to the substitution of Ti in the structure.

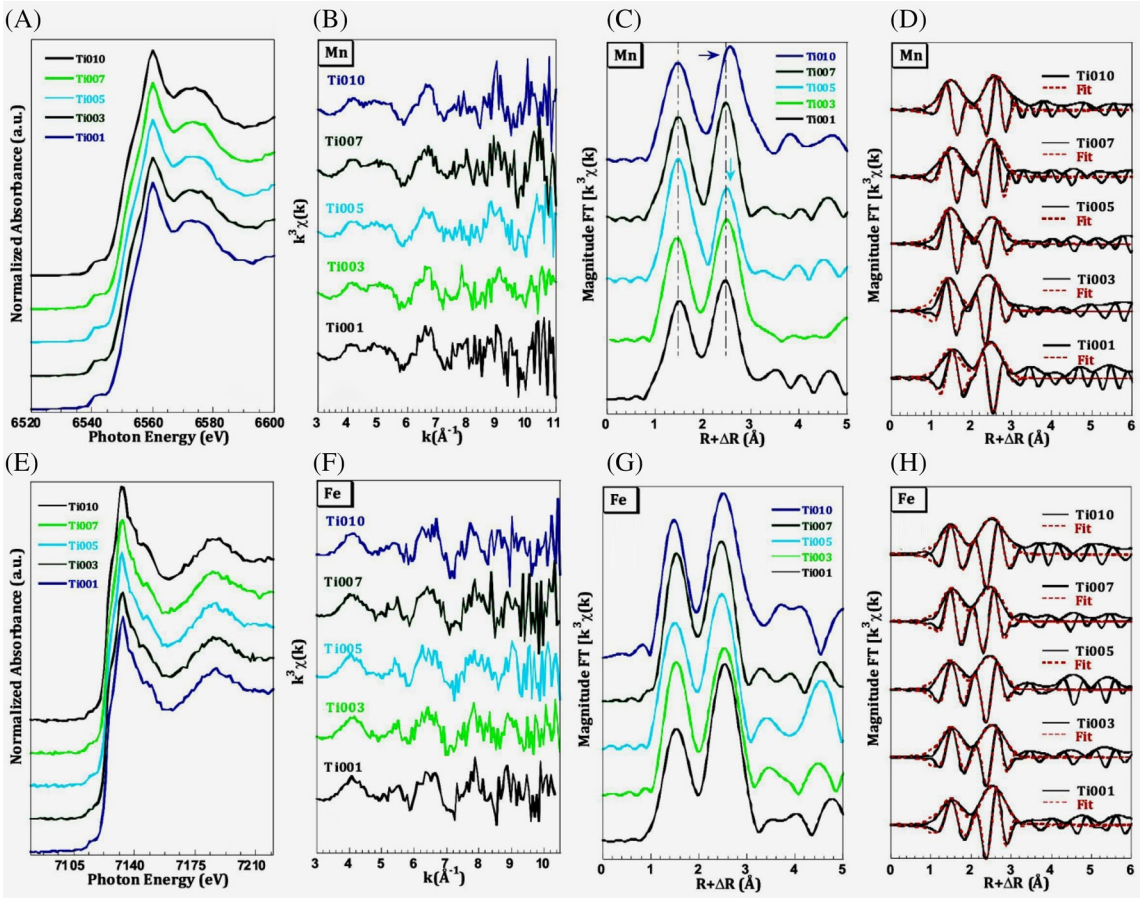


FIGURE 5 (A) and (E) XANES of Mn and Fe K-edge of Ti-substituted materials, respectively, and (B) and (F) the k^3-k graphs of Mn and Fe, (c), (D) and (G), (H) are Magnituted FT of Mn and Fe in Ti-substituted samples and fitting curves, respectively [Colour figure can be viewed at wileyonlinelibrary.com]

TABLE 1 FT results of Mn K-edge XANES spectra of the samples

Sample	Ligand	N (atom)	*R* (Å)	σ^2 (Å^2)	Δ*E* (eV)
Mn K-edge					
NMF_Ti001	Mn-O	2.6	1.91	0.00116	1.74
	Mn-M	4.6	2.91	0.00622	
NMF_Ti003	Mn-O	3.6	1.86	0.003219	−2.92
	Mn-M	4.0	2.88	0.004624	
NMF_Ti005	Mn-O	3.2	1.90	0.00184	4.47
	Mn-M	4.0	2.94	0.00755	
NMF_Ti007	Mn-O	2.4	1.90	0.000843	−0.16
	Mn-M	2.7	2.91	0.001147	
NMF_Ti010	Mn-O	2.6	1.92	0.001933	8.11
	Mn-M	2.8	2.96	0.001881	

Note: M may be Fe, Mn, or Ti.

Although we substituted Ti ions with Fe in $Na_{0.67}Mn_{0.5}Fe_{0.5}O_2$, we found that Ti^{4+} ions were substituted for both Mn and Fe sites in the lattice and caused an increase in 3+ ions due to the charge equilibrium in the structure. It should be noted that Mn and Fe in $Na_{0.67}Mn_{0.5}Fe_{0.5}O_2$ have the same site in the lattice,

TABLE 2 FT results of Fe K-edge XANES spectra of the samples

Sample	Ligand	N (atom)	R (Å)	σ^2 (Å^2)	ΔE (eV)
Fe K edge					
NMF_Ti001	Fe-O	3.0[f]	1.99	0.011202	4.66
	Fe-O	3.0[f]	2.06	0.011202	
	Fe-M	3.0[f]	2.93	0.004804	
NMF_Ti003	Fe-O	3.0[f]	1.99	0.009157	3.97
	Fe-O	3.0[f]	2.05	0.009157	
	Fe-M	3.0[f]	2.93	0.002409	
NMF_Ti005	Fe-O	4.3	1.99	0.005383	−1.33
	Fe-M	5.8	2.91	0.008028	
NMF_Ti007	Fe-O	3.3	1.99	0.001197	−0.72
	Fe-M	5.2	2.90	0.006814	
NMF_Ti010	Fe-O	4.2	2.00	0.005579	2.40
	Fe-M	5.9	2.95	0.007254	

Note: M may be Fe, Mn, or Ti.

and we concluded that Ti ions were substituted with both ions in the structure or Ti-substitution triggered the change in the valence state of the Mn ions in the lattice.

Figure 6A shows the CV graphs of Ti-substituted samples at a scan rate of 0.1 mV/s from 1.5 V to 4.0 V. The first charging peaks were obtained at 2.43 V. Ti-substitution caused an increase in the charging voltage, and the highest charging voltage reached 2.78 V ($\Delta V = 0.35$ V). Therefore, it is clear that Ti-substitution caused an increase in the chemical potential of the materials, which is important for the working voltage of the battery cells. Similarly, a decrease in the voltage of the redox peaks during the discharge from 2.11 V to 1.93 V in the structure was observed. In addition, the shoulder around 2.7 V was obtained more clearly by increasing the Ti content. So, it was concluded that the general structure of the CV graph of the pure material did not change with Ti-substitutions, as compared to that performed in other studies.[48,49]

It is well known that the diffusion rate of Na-ions has a crucial role in battery performance. The best battery performance was obtained for x = 0.07 Ti-substituted sample, and the CV of x = 0.07 for different scan rates was presented in Figure 6B. The diffusion coefficient can be calculated using Randles-Sevcik equation as given below[50,51]:

$$I_p = 2.69 \times 10^5 n^{3/2} A D_{Na^+}^{1/2} C_{Na} v^{1/2}$$

where n is the number of electrons, A is the surface area obtained from BET analysis as 0.68 m^2/g, D is the diffusion coefficient of Na^+ ions, C_{Na} is the concentration of Na ions in the Cathode, and v is the scan rate. The peak values in the CV measurements were determined depending on the scanning rate, as given in the inset of Figure 6B, and the D value was calculated from the slope of the data that was found to be 1.3×10^{-9} cm^2/s. The calculated diffusion coefficient of $Na_{0.67}Fe_{0.5}Mn_{0.5}O_2$ battery cell was reviewed in the literature and was found D = 10^{-12}–10^{-11} cm^2/s.[20] Furthermore, Bai et al investigated the fabrication temperature dependence of the diffusion coefficient, and it was found that D changes from 1.17×10^{-13} to 6.28×10^{-14} cm^2/s.[52] Similarly, Nayak et al found the D value is equal to 2.93×10^{-14} cm^2/s.[53] So, differences of the diffusion coefficient depending on the studies may be due to the differences in the fabrication conditions, voltage window, and used equation, etc. The calculated D value of x = 0.07 is better than that of the pure cathode which means a better battery performance.

The cycling performance of the battery cells fabricated using Ti-substituted $Na_{0.67}Mn_{0.5}Fe_{0.5}O_2$ was evaluated for up to 100 cycles for the C/3-rate, and the voltage range chosen was 1.5-4 V. Figure 7A presents the voltage–capacity graphs of the x = 0.07 sample, which shows the best battery performance among the samples. The first capacity value was obtained as 123.5 mAh/g, and it was decreased to 90.2 mAh/g for the 100th cycle. The cycle dependence of the capacities for all cells is presented in Figure 7B, and it is seen that Ti-substitution improved the capacity decrease in the cells. Figure 7C shows the 1st and 100th capacity values, depending on the Ti content. Although it is seen that the first capacity

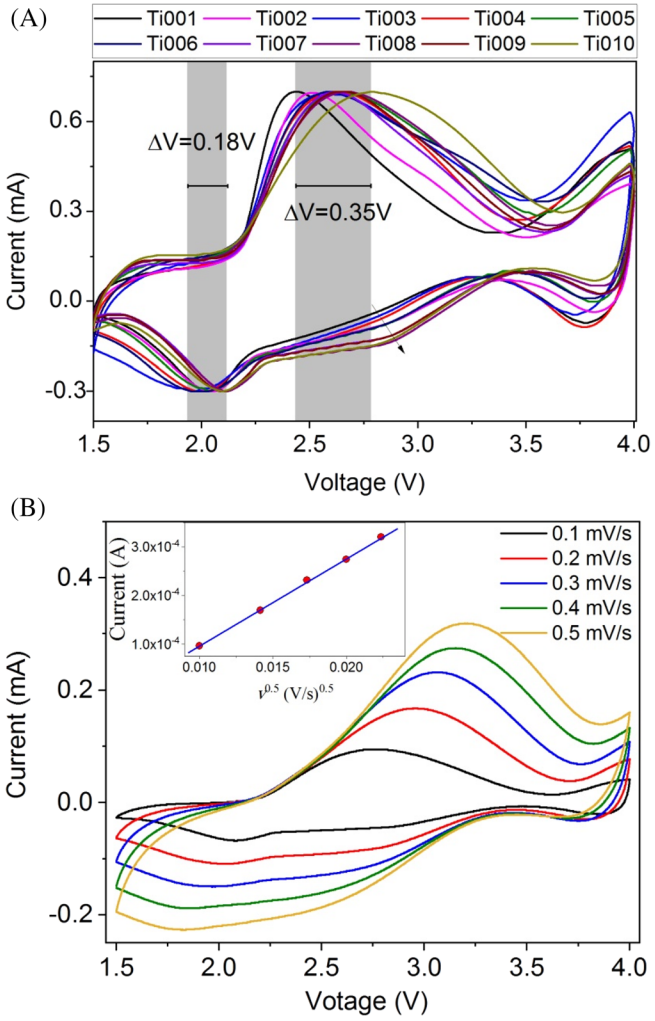


FIGURE 6 (A) CV of Ti-substituted $Na_{0.67}Fe_{0.5}Mn_{0.5}O_2$where x = 0.01–0.1 and (B) CV graph of x = 0.07 for different scan rates. The inset in Figure 6B shows the current-$\nu^{0.5}$ graphs for diffusion calculation [Colour figure can be viewed at wileyonlinelibrary.com]

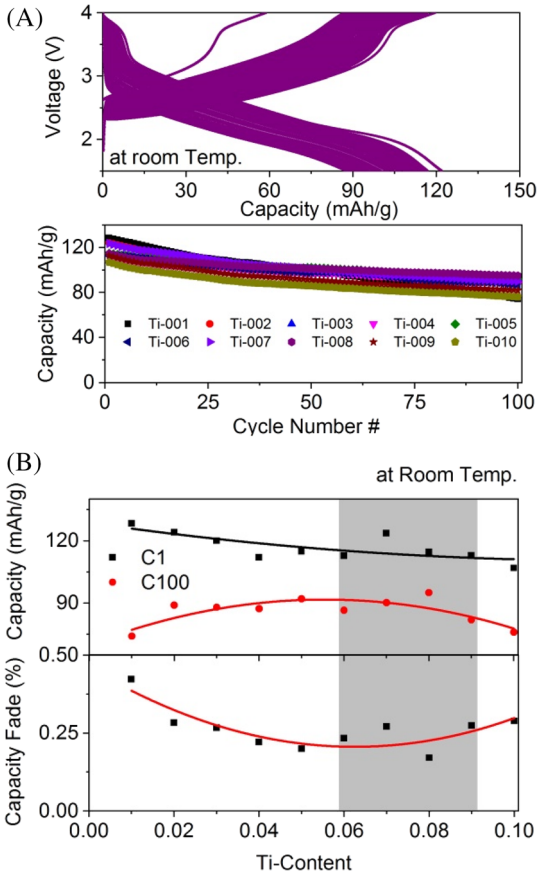


FIGURE 7 Capacity–voltage graphs for (A) x = 0.07, (B) capacity–cycle graphs of Ti-substituted samples, and (C) the first and 100th capacities and capacity fade of Ti-substituted cells [Colour figure can be viewed at wileyonlinelibrary.com]

decreased from 128.4 mAh/g to 106 mAh/g with increasing Ti content, the capacity values for the 100th cycle demonstrated a parabolic change in the structure. Therefore, it was predicted that the best performance was obtained for the range of x = 0.06-0.09 Ti-substitution. The capacity fade of the cells is presented in Figure 7D, and it is seen that the best performance was obtained for x = 0.07 in the cells. Table 3 presents the studies in the literature about $Na_{0.67}Mn_{0.5}Fe_{0.5}O_2$ cathodes, and it is seen that the voltage window and C-rates directly affect the capacity and capacity fade of the cells. The highest capacity obtained was 200 mAh/g for the C/20-rate, and the lowest capacity fade was 0.125 for 50 cycles.[10] The nanofiber $Na_{0.67}Mn_{0.5}Fe_{0.5}O_2$ showed high capacity and capacity fade when compared to the other production methods due to the surface area.[52] The galvanostatic cycling measurements over 100 cycles showed a capacity fade of 0.485 for the range of 1.5 to 4.2 V.[16] So, the Ti-substituted samples presented better battery performance when compared to the samples described in other similar studies, as given in Table 3. Park et al investigated the Ti-substitution effect for both Mn and Fe sites in $Na_{2/3}Mn_{0.5}Fe_{0.5}O_2$ materials, and they claimed that there are slight differences in the electrochemical performance of the cells and that Fe-site substitution results in better cycling capability of the cells. They also described the mechanism of the Ti ions in the structure.[26] Although they substituted Ti in $Na_{0.67}Mn_{0.5}Fe_{0.5}O_2$ in the structure and found better results when compared to the undoped samples, they only used x = 0.05 and x = 0.1 as the Ti levels in the structure. We systematically investigated the Ti-substitution effect and found that x = 0.6-0.9 gives better performance when compared to all other samples.

It is well known that the battery performance of the cells is directly related to the environmental temperature, and it is important to determine the change in the capacity and capacity fade depending on the environmental

TABLE 3 The electrochemical properties of $Na_{2/3}Mn_{0.5}Fe_{0.5}O_2$. The bold values indicate the results in this study.

First Capacity	Applied Current	Voltage Window	Capacity Fade	Ref.
~143	unwriten	1.5-3.8	-	49
110	13 mA/g	1.5-4	0.182 for 50 cycles (13 mA/g)	48
~160	C/10 (1C = 200)	1.5-4	0.125 for 50 cycles	18
119.9	130 mA/g	1.5-4	~0.17 for 40 cycles	47
175	C/5	1.5-4	-	54
120	C/2	1.5-4	-	17
171.3	C/2	1.5-4.2	-	55
129.1	1C	1.5-4.2	-	56
~125	C/5	1.5-4.2	~0.59 for 50 cycles (c/10)	57
~131.9	1C	1.5-4.2	0.107 for 130 cycles (C/10) nanofiber	52
~550 wh/kg	C/20	1.5-4.3	~0.27 for 30 cycles	11
200	C/20	1.5-4.3	0.35 for 50 cycles (C/20)	**10**
119	C/10	2-4	0.18 for 25 cycles (C/10)	58
130	130mAh/g	2-4.2	0.485 for 100 cycles	**20**
~135	100 mA/g	2-4.3	~0.72 for 200 cycles İonic elecrrolyte	59
190	C/20	1.5-4.2	0.23 for 100 cycle Ti-substitutiun	19
123.5	**C/3**	**1.5-4**	**0.17 for 100 cycle x = 0.07 Ti substitution**	**in this study**

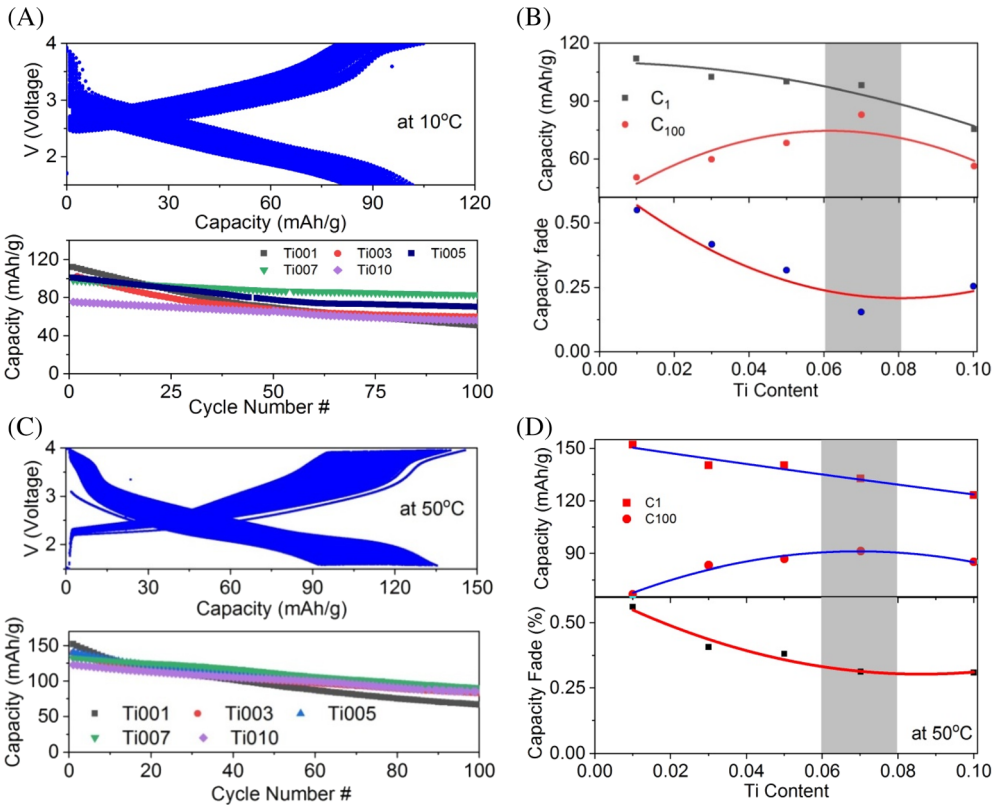


FIGURE 8 Temperature dependence of (a) the voltage–capacity for x = 0.07 up to 100 cycle at 10°C (up panel) and, capacity–cycle number graphs for x = 0.01, 0.03, 0.005, 0.07, and 0.10 at 10°C (down panel), (b) the capacity of the first and 100th and capacity fades for x = 0.01, 0.03, 0.005, 0.07, and 0.10 at 10°C, (c) the voltage–capacity for x = 0.07 up to 100 cycle at 50°C (up panel) and, capacity–cycle number graphs for x = 0.01, 0.03, 0.005, 0.07, and 0.10 at 10°C (down panel), (d) the capacity of the first and 100th and capacity fades for x = 0.01, 0.03, 0.005, 0.07, and 0.10 at 50°C [Colour figure can be viewed at wileyonlinelibrary.com]

temperature. The lower limit and upper limit of the environmental temperature were chosen as 10°C and 50°C, respectively, due to the electrolytes in the cells. The dependence of the battery performance on the temperature was determined for the C/2 rate. Figure 8A shows the capacity–voltage graph of the battery cells (upper

panel) at 10°C for x = 0.07with the best performance at room temperature and the capacity change with the cycle number (down panel) for x = 0.01, 0.03, 0.05, 0.07, and 0.10 for 10°C. The first capacity was found to be 97.9 mAh/g, which was reduced to 83.6 mAh/g, and the capacity fade was calculated as 0.15 for 100 cycles.

Figure 8B shows the changes of the first and 100th capacity values (upper panel) and the capacity fade (down panel) with Ti-content for 10°C. The lowest capacity value was obtained for x = 0.1, and the best performance was obtained for x = 0.07. When the capacity values were compared to room-temperature measurements, a decrease in the values was seen. Although the measurement was performed for C/2 rates, the decrease with the change in environmental temperature should be due to the decrease in the mobility of the Na ions in the electrolyte. **Figure 8**C shows the capacity–voltage graph (upper panel) of the battery cells at 50°C for x = 0.07 and the capacity change with the cycle number (down panel) for x = 0.01, 0.03, 0.05, 0.07, and 0.10 for 50°C. The first capacity value was found to be 132.5 mAh/g, decreasing to 93 mAh/g for the last cycle for x = 0.07 cells at 50°C. Although the highest capacity value for the first cycle was obtained for x = 0.01, the best capacity values for the 100th cycle were obtained for x = 0.07 Ti-substituted cells. Figure 8D presents the first and 100th capacity values (upper panel) and capacity fade values (down panel) depending on the Ti-content in the structure, and it is seen that the best value was obtained for x = 0.07 cells. Therefore, it is predicted that Ti-substitution between x = 0.06 and x = 0.08 gives optimum values for battery applications. In addition, it should be noted that the increase in the mobility of the Na ions causes an increase in the capacity of the cells, which is directly affected by environmental conditions.

Figure 9 presents the C-rate capability of the battery cells at room temperature. It was found that Ti-substitution at a low level results in better performance for low C-rates, and the increasing C-rate causes better performance for high levels of Ti-substitutions. A similar observation was obtained in the study by Park et al,[19] and it was found that Ti ions increase the structural stability during the cycling of the battery cells, which should be due to the higher bonding energy of Ti-O.[19]The C-rate of the battery cells is directly related to the diffusion rate of the Na-ions and the NaO_2 slab size. Similar results were obtained by Li et al, and they stated that the enhanced rate capability at high rates is related to disorder in the transition metal layer and prevents Na + ion/vacancy ordering in the structure.[60,61] So, the results in this study confirms the discussion given above.

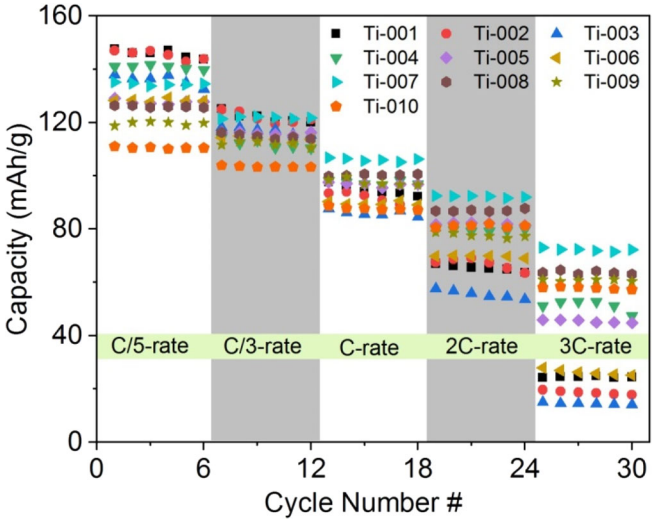


FIGURE 9 C-rate values of Ti-substituted $Na_{0.67}Fe_{0.5}Mn_{0.5}O_2$ cells [Colour figure can be viewed at wileyonlinelibrary.com]

4 | CONCLUSION

$Na_{0.67}Mn_{0.5}Fe_{0.5-x}Ti_xO_2$ samples were successfully produced by modifying the solid-state reaction process. According to the XRD analysis, the powders had no impurity phases and they had P63/mmc symmetry. The lattice volume increased with increasing Ti-substitution, which may cause Na ions to move more easily during charging and discharging. From the SEM images, it was found that the grain size increased with increasing Ti content in the samples. The FTIR spectra of the samples showed that Ti-substitution did not cause a drastic change in the structure. It was concluded from the XANES spectra that Ti^{4+} substitution with Fe ions should increase the number of Fe^{3+} ions and decrease the number of Fe^{4+} ions in the structure. The metal–oxygen bond length after Ti-substitution was investigated, and a slight change in the structure was found. The CV graphs of Ti-substituted samples were almost the same as the pure sample, and it is suggested that the Ti ions in the cells may not change the cycling mechanism of the Na ion. According to galvanostatic cycling measurements at room temperature, the best performance was obtained for the range of x = 0.06-0.09 Ti-substitution in the structure. The environmental temperature effect in the battery cells was determined at 10°C and 50°C, and it was found that the Ti-substituted cells may be used in the range of 10 to 50°C in this configuration. In conclusion, Ti ions have a crucial role in the improvement of the electrochemical performance of $Na_{0.67}Mn_{0.5}Fe_{0.5}O_2$ materials, and they may have also a crucial role in the improvement of battery performance of Na-ion cells. So, it should be

discussed that a certain number of Ti-substitution in $Na_{0.67}Mn_{0.5}Fe_{0.5}O_2$ gives better battery performance when compared with the unsubstituted sample. So, the mechanism can be discussed with basic force in nature. It is seen that the crucial number of impurity ions in the lattice causes the improvement of the Na-diffusion rate during the charge and discharge. In this case, the electrostatic force of the substituted ions which have a different charge value from original ions will change and it may increase the stability of the lattice during cycling. When the Na-ions removed to the lattice, the remaining structure should protect their skeleton till came back of Na-ions. So, Ti^{4+} ions pull stronger the O^{2-} ions than that of Fe^{3+}, and it may protect the change of the lattice during to cycling.

ACKNOWLEDGMENT

Prof. Ali Bayri would like to thank to Inonu University Research council with contract number of FBA-2019-1857. Prof. S. Altin would like to thank SESAME for XAS experiments with project number of 20185036. We also want to thank EU CALIPSO program for travelling and accommodation support during the SESAME experiments. Prof. S. Altin would like to thank TUBITAK for financial support by the contract number of 119M169.

ORCID

Serdar Altin https://orcid.org/0000-0002-4590-907X
Erdinc Oz https://orcid.org/0000-0003-4321-8264

REFERENCES

1. Farhad S, Nazari A. Introducing the energy efficiency map of lithium-ion batteries. *Int J Energy Res*. 2019;43:931-944.
2. Kumar D, Nema RK, Gupta S. A comparative review on power conversion topologies and energy storage system for electric vehicles. *Int J Energy Res*. 2020; in press. https://doi.org/10.1002/er.5353.
3. Zhu Y, Nie W, Chen P, Zhou Y, Xu Y. Li-doping stabilized P2-$Li_{0.2}Na_{1.0}Mn_{0.8}O_2$ sodium ion cathode with oxygen redox activity. *Int J Energy Res*. 2020;44:3253-3259.
4. Zhu L, Ding G, Xie L, Yang Q, Yang X, Cao X. Facile preparation of NaV_3O_8/polytriphenylamine composites as cathode materials towards high-performance sodium storage. *Int J Energy Res*. 2020;44:3215-3223.
5. Zhu L, Sun Q, Xie L, Cao X. $Na_3V_2(PO_4)_3$@NC composite derived from polyaniline as cathode material for high-rate and ultralong-life sodium-ion batteries. *Int J Energy Res*. 2020;44:4586-4594.
6. Lee Y, Kim S-O, Kim H-S, Yu S. Thermodynamic analysis of high energy density conversion type cathode materials for Na- and K-ion batteries. *Int J Energy Res*. 2020;44:6068-6077.
7. Saurel D, Galceran M, Reynaud M, Anne H, Casas-Cabanas M. Rate dependence of the reaction mechanism in olivine $NaFePO_4$ Na-ion cathode material. *Int J Energy Res*. 2018;42:3258-3265.
8. Zhan W-X, Fan C-L, Zhang W-H, et al. Ultra-long cycle life and high rate performance subglobose $Na_3V_2(PO_4)_2F_3$ @C cathode and its regulation. *Int J Energy Res*. 2020; Article in press. https://doi.org/10.1002/er.5397.
9. Yabuuchi N, Kajiyama M, Iwatate J, et al. P2-type $Na_x[Fe_{1/2}Mn_{1/2}]O_2$ made from earth-abundant elements for rechargeable NaÂ batteries. *Nat Mater*. 2012;11:512-517.
10. Duffort V, Talaie E, Black R, Nazar LF. Uptake of CO_2 in layered P2-$Na_{0.67}Mn_{0.5}Fe_{0.5}O_2$: insertion of carbonate anions. *Chem Mater*. 2015;27:2515-2524.
11. Talaie E, Duffort V, Smith HL, Fultz B, Nazar LF. Structure of the high voltage phase of layered P2-$Na_{2/3-z}[Mn_{1/2}Fe_{1/2}]O_2$ and the positive effect of Ni substitution on its stability. *Energ Environ Sci*. 2015;8:2512-2523.
12. Kubota K, Komaba S. Review—practical issues and future perspective for Na-ion batteries. *J Electrochem Soc*. 2015;162:A2538-A2550.
13. Ding C, Nohira T, Hagiwara R. Charge-discharge performance of $Na_{2/3}Fe_{1/3}Mn_{2/3}O_2$ positive electrode in an ionic liquid electrolyte at 90 °C for sodium secondary batteries. *Electrochim Acta*. 2017;231:412-416.
14. Singh G, López Del Amo JM, Galceran M, Pérez-Villar S, Rojo T. Structural evolution during sodium deintercalation/intercalation in $Na_{2/3}[Fe_{1/2}Mn_{1/2}]O_2$. *J Mater Chem A*. 2015;3:6954-6961.
15. Altin E, Altundag S, Altin S, Bayri A. Fabrication of Cr doped $Na_{0.67}Fe_{0.5}Mn_{0.5}O_2$ compounds and investigation of their structural, electrical, magnetic and electrochemical properties. *J Mater Sci Mater Electron*. 2019;30:17848-17855.
16. Marelli E, Villevieille C, Park S, Hérault N, Marino C. Co-free P2-$Na_{0.67}Mn_{0.6}Fe_{0.25}Al_{0.15}O_2$ as promising cathode material for sodium-ion batteries. *ACS Appl Energy Mater*. 2018;1(1):5960-5967.
17. Kong W, Wang H, Sun L, Su C, Liu X. Understanding the synergic roles of MgO coating on the cycling and rate performance of $Na_{0.67}Mn_{0.5}Fe_{0.5}O_2$ cathode. *Appl Surf Sci*. 2019;497:143814.
18. Wang H, Gao R, Li Z, Sun L, Hu Z, Liu X. Different effects of Al substitution for Mn or Fe on the structure and electrochemical properties of $Na_{0.67}Mn_{0.5}Fe_{0.5}O_2$ as a sodium ion battery cathode material. *Inorg Chem*. 2018;57:5249-5257.
19. Park JK, Park GG, Kwak HH, Hong ST, Lee JW. Enhanced rate capability and cycle performance of titanium-substituted P2-type $Na_{0.67}Fe_{0.5}Mn_{0.5}O_2$ as a cathode for sodium-ion batteries. *ACS Omega*. 2017;3:361-368.
20. Chu S, Chen Y, Wang J, et al. A cobalt and nickel co-modified layered P2-$Na_{2/3}Mn_{1/2}Fe_{1/2}O_2$ with excellent cycle stability for high-energy density sodium-ion batteries. *J Alloys Compd*. 2019;775:383-392.
21. Bayri A., Gocer E., Altin E., Altundag S., Oz E., Harfouche M., Altin S., S. Avci, $Ni_{0.8}Co_{0.15}Ti_{0.05}O_2$: Synthesis by solid state reaction and investigation of structural and electrochemical properties with enhanced battery performance, Under Review
22. Guo Z, Wang D, Zhang L, Fu Q, Wei Y. Titanium-substituted Tavorite $LiFeSO_4F$ as cathode material for lithium ion batteries: first-principles calculations and experimental study. *ChemPlusChem*. 2020;85:900-905.
23. Weigel T, Schipper F, Erickson EM, Susai FA, Markovsky B, Aurbach D. Structural and electrochemical aspects of

$LiNi_{0.8}Co_{0.1}Mn_{0.1}O_2$ cathode materials doped by various cations. *ACS Energy Lett*. 2019;4:508-516.
24. Toby BH, Von Dreele RB. GSAS-II: the genesis of a modern open-source all purpose crystallography software package. *J Appl Cryst*. 2013;46:544-549.
25. Toby BH. EXPGUI, a graphical user interface for GSAS. *J Appl Cryst*. 2001;34:210-213.
26. Su H, Jaffer S, Yu H. Transition metal oxides for sodium-ion batteries. *Energy Storage Mater*. 2016;5:116-131.
27. Zhang R, Cui Y, Fan W, He G, Liu X. Ambient stable $Na_{0.76}Mn_{0.48}Ti_{0.44}O_2$ as anode for Na-ion battery. *Electrochim Acta*. 2019;295:181-186.
28. Augustin M, Fenske D, Bardenhagen I, et al. Manganese oxide phases and morphologies: a study on calcination temperature and atmospheric dependence. *Beilstein J Nanotechnol*. 2015;6:47-59.
29. Shannon RD. Revised effective ionic radii and systematic studies of interatomic distances in halides and chalcogenides. *Acta Crystallogr section A*. 1976;A32:751-767.
30. Ahrens LH. The use of ionization potentials. Part 1. Ionic radii of the elements. *Geochim Cosmochim Acta*. 1952;2:155-169.
31. Ahangaran F, Hassanzadeh A, Nouri S. Surface modification of Fe_3O_4@SiO_2 microsphere by silane coupling agent. *Int Nano Lett*. 2013;3:23.
32. Mozgawa W, Król M, Barczyk K. FT-IR studies of zeolites from different structural groups. *Chemik*. 2011;65:667-674.
33. Sommerfeld M, Schmalfuß S. Analysis and optimisation of particle mixing performance in fluid phase resonance mixers based on Euler/Lagrange calculations. *Adv Powder Technol*. 2020;31:139-157.
34. Dos Santos Pereira AP, Da Silva MHP, Lima ÉP, Dos Santos Paula A, Tommasini FJ. Processing and characterization of PET composites reinforced with geopolymer concrete waste. *Mater Res*. 2017;20:411-420.
35. Dimitrakopoulou M, Huang X, Kröhnert J, et al. Insights into structure and dynamics of (Mn,Fe)O: X-promoted Rh nanoparticles. *Faraday Discuss*. 2018;208:207-225.
36. NIST Standard Reference Database Number 69, DOI: https://doi.org/10.18434/T4D303
37. Abràmoff MD, Magalhães PJ, Ram SJ. Image processing with imageJ. *Biophotonics Int*. 2003;11:36-42.
38. Collins TJ. ImageJ for microscopy. *Biotechniques*. 2007;43:1s.
39. Schneider CA, Rasband WS, Eliceiri KW. NIH image to ImageJ: 25 years of image analysis. *Nat Methods*. 2012;9:671-675.
40. He J., *Metal Oxide Varistors: from Microstructure to Macro-Characteristics*. Weinheim, Germany: Willey VCH, 2019, ISBN: 978-3-527-33382-0
41. Hng HH, Halim L. Grain growth in sintered ZnO–1 mol% V_2O_5 ceramics. *Mater Lett*. 2003;57:1411-1416.
42. Sikora M, Kapusta C, Knížek K, et al. X-ray absorption near-edge spectroscopy study of Mn and Co valence states in $LaMn_{1-x}Co_xO_3$ (x = 0–1). *Phys Rev B*. 2006;73:094426.
43. Saratovsky I, Wightman PG, Paste PA, Gaillard J-F, Poeppelmeier KR. Manganese oxides: parallels between abiotic and biotic structures. *J Am Chem Soc*. 2006;128:11188-11198.
44. Manceau A, Marcus MA, Grangeon S. Determination of Mn valence states in mixed-valent manganates by XANES spectroscopy. *Am Mineral*. 2012;97:816-827.
45. Marcus MA, Westphal AJ, Fakra SC. Classification of Fe-bearing species from K-edge XANES data using two-parameter correlation plots: Erratum. *J Synchrotron Rad*. 2009;16:439.
46. Galdenzi F., G. D. Ventur, Cibin G., Macis S., Marcelli A., Accurate Fe^{3+}/Fetot ratio from XAS spectra at the Fe K-edge, *Radiation Physics and Chemistry*. 2020;175 108088https://doi.org/10.1016/j.radphyschem.2018.12.008
47. Bai Y, Zhao L, Wu C, Li H, Li Y, Wu F. Enhanced sodium ion storage behavior of P2-type $Na_{2/3}Fe_{1/2}Mn_{1/2}O_2$ synthesized via a chelating agent assisted route. *ACS Appl Mater Interfaces*. 2016;8:2857-2865.
48. Xu J, Chou SL, Wang JL, Liu HK, Dou SX. Layered P2-$Na_{0.66}Fe_{0.5}Mn_{0.5}O_2$ cathode material for rechargeable sodium-ion batteries. *ChemElectroChem*. 2014;1:371-374.
49. Mortemard de Boisse B, Carlier D, Guignard M, Delmas C. Structural and electrochemical characterizations of P2 and new O3-$Na_xMn_{1-y}Fe_yO_2$ phases prepared by auto-combustion synthesis for Na-ion batteries. *J Electrochem Soc*. 2013;160:A569-A574.
50. Jia M, Zhang Y, Tian H, Su Z. Synthesis and electrochemical performance of $Na_{3-x}Li_xV_2(PO_4)_3$/C as cathode materials for Li-ion batteries. *Int J Energy Res*. 2019;43:6004-6012.
51. Karuppiah D, Palanisamy R, Ponnaiah A, Rengapillai S, Marimuthu S. Cobalt-doped layered lithium nickel oxide as a three-in-one electrode for lithium-ion and sodium-ion batteries and supercapacitor applications. *Int J Energy Res*. 2020;44:7591-7602.
52. Guan M, Chen J, Zhang X, Yang L, Wang B, Zhong S. Yarn-ball-shaped P2-$Na_{2/3}Fe_{1/2}Mn_{1/2}O_2$ nanofibers prepared by magnetic-assisted electrospinning method as high-performance cathode material for Na-ion batteries. *Mater Lett*. 2019;254:24-27.
53. Nayak D, Sarkar T, Chaudhary NVP, Bharadwaj MD, Ghosh S, Adyam V. Electrochemical properties and first-principle analysisof $Na_x[M_yMn_{1-y}]O_2$ (M = Fe, Ni) cathode. *J Solid State Electrochem*. 2018;22:1079-1089.
54. Moeez I, Jung HG, Lim HD, Chung KY. Presodiation strategies and their effect on electrode-electrolyte interphases for high-performance electrodes for sodium-ion batteries. *ACS Appl Mater Interfaces*. 2019;11:41394-41401.
55. Sui Y, Hao Y, Zhang X, et al. Spray-drying synthesis of P2-$Na_{2/3}Fe_{1/2}Mn_{1/2}O_2$ with improved electrochemical properties. *Adv Powder Technol*. 2020;31:190-197.
56. Chen J, Zhong S, Zhang X, et al. High performance of hexagonal plates P2-$Na_{2/3}Fe_{1/2}Mn_{1/2}O_2$ cathode material synthesized by an improved solid-state method. *Mater Lett*. 2017;202:21-24.
57. Viswanatha R, Kishore B, Bharath U, Munichandraiah N. Communication—electrochemical investigation of plate-like Na 2/3 Fe 1/2 Mn 1/2 O 2 for sodium ion cathode. *J Electrochem Soc*. 2018;165:A263-A265.
58. Han MH, Acebedo B, Gonzalo E, et al. Synthesis and electrochemistry study of P2- and O3-phase $Na_{2/3}Fe_{1/2}Mn_{1/2}O_2$. *Electrochim Acta*. 2015;182:1029-1036.
59. Ding C, Nohira T, Hagiwara R. Charge-discharge performance of $Na_{2/3}Fe_{1/3}Mn_{2/3}O_2$ positive electrode in an ionic liquid electrolyte at 90 °C for sodium secondary batteries. *Electrochim Acta*. 2017;231:412-416.

60. Li Z.-Y., Gao R., Zhang J., Zhang X., Hu Z., Liu X., New insights into designing high-rate performance cathode materials for sodium ion batteries by enlarging the slab-spacing of the Na-ion diffusion layer. *J Mater Chem A* 2016; 4:3453−3461
61. Li Z-Y, Gao R, Sun L, Hu Z, Liu X. Zr-doped P2-$Na_{0.75}Mn_{0.55}Ni_{0.25}Co_{0.05}Fe_{0.10}Zr_{0.05}O_2$ as high-rate performance cathode material for sodium ion batteries. *Electrochim Acta*. 2017;223:92-99.

How to cite this article: Altin S, Altundag S, Altin E, Oz E, Harfouche M, Bayri A. Investigation of Ti-substitution effects on structural and electrochemical properties of $Na_{0.67}Mn_{0.5}Fe_{0.5}O_2$ battery cells. *Int J Energy Res*. 2020;1–13. https://doi.org/10.1002/er.5820